ACS Catalysis

Research Article

pubs.acs.org/acscatalysis

Energy of Supported Metal Catalysts: From Single Atoms to Large Metal Nanoparticles

Trevor E. James, Stephanie L. Hemmingson, and Charles T. Campbell*

Department of Chemistry, University of Washington, Box 351700, Seattle, Washington 98195-1700 United States

ABSTRACT: Many catalysts consist of late transition metal nanoparticles dispersed across oxide supports. The chemical potential of the metal atoms in these particles correlate with their catalytic activity and long-term thermal stability. This chemical potential versus particle size across the full size range between the single isolated atom and bulklike limits is reported here for the first time for any metal on any oxide. The chemical potential of Cu atoms on $CeO_2(111)$ surfaces, determined by single crystal adsorption calorimetry of gaseous Cu atoms onto slightly reduced $CeO_2(111)$ at 100 and 300 K is shown to decrease dramatically with increasing Cu cluster size. The Cu chemical potential is ~110 kJ/mol higher for isolated Cu adatoms on stoichiometric terrace sites than for Cu in nanoparticles exceeding 2.5 nm diameter, where it reaches the bulk Cu(solid) limit. In Cu dimers, Cu's chemical potential is ~57 kJ/mol lower at step edges than on stoichiometric terrace sites. Since Cu avoids oxygen vacancies, these monomer and dimer results are not strongly influenced by the 2.5% oxygen vacancies present on this CeO_2 surface and are thus considered representative of stoichiometric $CeO_2(111)$ surfaces.

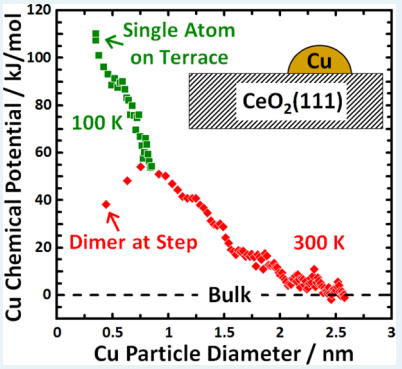

KEYWORDS: *catalysis, adsorption energy, ceria, copper, nanoparticles, size effects*

1. INTRODUCTION

Late transition metal nanoparticles dispersed across oxide supports form the basis of industrially important heterogeneous catalysts and are the subject of intensive research.[1−15] The strength of bonding of the metal to the oxide support has been shown to control the chemical potential of the metal atoms in the nanoparticles and how it varies with particle size.[11−14] This chemical potential in turn influences how strongly adsorbed catalytic reaction intermediates bind to the metal particles[13] and how quickly the particles deactivate by sintering.[11,15] Thus, understanding the strength of bonding of late transition metals to oxide support and the resulting metal chemical potential is crucial for understanding structure−function relationships in catalysis. However, no one has previously reported an experimental measurement of the adsorption energy of any late transition metal adsorbed in the form of isolated atoms on any oxide surface. We report here calorimetric measurements of the adsorption energies of Cu atoms onto $CeO_2(111)$ under conditions where they remain as isolated adatoms on terraces and others where they grow as Cu nanoparticles with controllable average size. We estimate from these Cu's chemical potential versus particle size across the full range from single Cu adatoms to the bulk Cu(solid) limit. This has never been reported for any late transition metal on any oxide surface and provides a simple benchmark for validating the energy accuracy of quantum mechanical calculations of metal/oxide bonding, for example, density functional theory (DFT).[9,10] These Cu/$CeO_2(111)$ model catalysts address the crucial role of ceria as a support[11,15−28] and of Cu nanoparticles in industrial catalysis.[6−8]

In this work, Cu was dosed onto a slightly reduced $CeO_2(111)$ surface at 100 K, and its heat of adsorption was measured by calorimetry, and the resulting structure of the adsorbed Cu and Cu nanoparticle size were characterized using surface spectroscopies. The results are compared with our previous study of Cu adsorption onto this same surface at 300 K, where Cu makes clusters at step edges, even at the lowest coverage studied.[29] Cooling to 100 K enables production of isolated Cu adatoms located on stoichiometric $CeO_2(111)$ terraces. We also compare these results with previous DFT+U studies of the adsorption energy of Cu atoms on stoichiometric and reduced $CeO_2(111)$ surfaces.[17−21]

2. EXPERIMENTAL SECTION

The microcalorimetry apparatus has been described in detail elsewhere.[30] The calorimeter was housed in an ultrahigh vacuum chamber, with a base pressure of ~2×10^{-10} mbar. It was equipped with low-energy electron diffraction, X-ray photoelectron spectroscopy (XPS), ion scattering spectroscopy (ISS), a quadrupole mass spectrometer (QMS), and two quartz crystal microbalances (QCM). ISS was performed using He^+ ions with a 1.5 kV primary energy, and XPS with Al Kα X-rays.

Single crystal adsorption calorimetry was performed as described in detail previously.[29−32] The calorimeter heat detector is a pyroelectric polyvinylidene fluoride (PVDF) ribbon that was translated into mechanical contact with the

Received: July 1, 2015
Revised: August 13, 2015
Published: August 14, 2015

DOI: 10.1021/acscatal.5b01372
ACS Catal. 2015, 5, 5673−5678

backside of the Pt sample. A 4 mm diameter beam of Cu atoms is chopped and collimated through a series of apertures to produce a spatially and temporally well-defined 100 ms pulse every 2 s that is directed onto the front face of the single crystal sample. The detector response is usually calibrated using pulses of a known energy from a HeNe laser before and after each calorimetry run, but here, we did not know the exact optical reflectivity of the ceria-coated Pt sample, which changes from run to run as a result of differences in ceria film thickness. Therefore, we scaled the absolute calibration factor slightly so that the multilayer heat of adsorption in the high-coverage limit equals the literature value for the heat of sublimation of bulk Cu(solid).

The $CeO_2(111)$-coated Pt(111) sample was cooled to 100 K for calorimetry by mounting both the sample holder and the calorimetry detector head on a liquid-nitrogen-cooled thermal reservoir. Its temperature was monitored by two type K thermocouples attached to the sample holder and the PVDF ribbon holder as close as possible to the Pt sample. Before each calorimetry measurement, the detector was retracted and the surface was flash-heated to 873 K (measured by optical pyrometry) in 1×10^{-6} Torr O_2 to remove adsorbed background gases. It recooled quickly (<3 min) to a stable temperature near 100 K, and calorimetry was begun. The Pt sample was mounted on a manipulator for XPS and ISS analysis and for transfer to and from the calorimetry position. The manipulator fork that holds the sample platen was cooled to 100 K by a reservoir of liquid nitrogen, and its temperature there was monitored by a type K thermocouple mounted to the manipulator fork as close as possible to the sample.

The absolute flux of Cu atoms was determined by QCMs, as described previously.[29,30] The sticking probability of the Cu atoms was measured with a QMS. See refs 30−32 for more details on measurement methods.

The growth morphology of Cu on $CeO_{2-x}(111)$ was determined using He^+ ISS detected normal to the surface at a 135° scattering angle, 2×10^{-7} Torr He background, and 3 mA emission current (which gives an ion current of ~90 nA/cm^2 averaged over the sample area over which the ion beam is rapidly rastered).

3. RESULTS

3.1. $CeO_2(111)$ Thin Film Characterization. The $CeO_2(111)$ thin films used were grown on a Pt(111) substrate and characterized as described previously.[29,33] They were grown to a thickness of 4 nm, which is twice the thickness needed to achieve bulklike heats of adsorption for Ag atoms.[33] The ceria oxidation state was verified by XPS of the Ce 3d region as described previously,[29] measuring the contribution of Ce^{3+} to the total integrated area of the 3d region $[Ce^{3+}]/([Ce^{3+}] + [Ce^{4+}])$.[34] This showed the CeO_2 surface to have ~2.5% oxygen vacancies (i.e., $CeO_{1.95}$), which are known to reside mainly at step edges[22] that cover ~5% of the surface.[29]

3.2. Cu Film Growth Morphology on $CeO_{1.95}(111)$ at 100 K. Discrete amounts of Cu were deposited onto $CeO_{1.95}(111)$ films at 100 K using the same Cu atomic beam as in the calorimetry experiments, and the Cu and Ce signals were monitored using He^+ ISS (Figure 1a). Total Cu coverage is defined in monolayers (ML), where 1 ML = 7.89×10^{14} atoms/cm^2, the density of O atoms in the top layer of $CeO_2(111)$. The integrated ISS intensity of the Cu was normalized to that from a thick enough Cu overlayer to block all the Ce signal (>40 ML). The Ce ISS signal was normalized

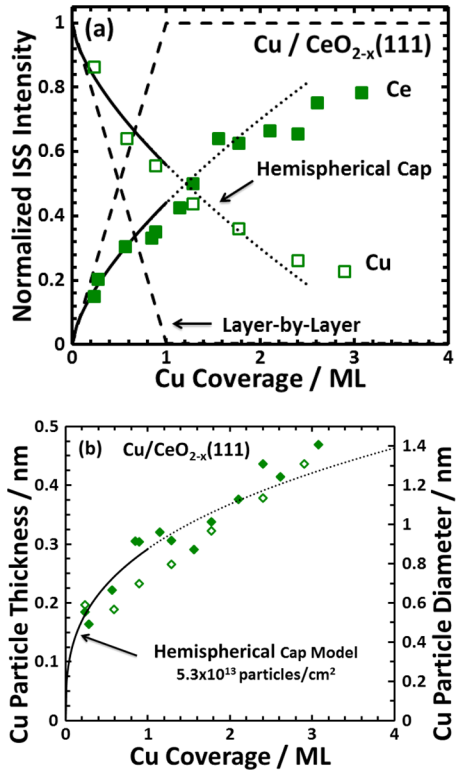

Figure 1. (a) Integrated Cu (closed) and Ce (open) ISS signal intensities normalized to bulklike (>40 ML) Cu and clean $CeO_{1.95}(111)$, respectively, as a function of total Cu coverage at 100 K onto $CeO_{1.95}(111)$. The dashed line represents a layer-by-layer fit for 2-dimensional growth of Cu. The solid line represents a hemispherical cap fit with a fixed particle density of 5.3×10^{13} particles/cm^2. (b) The average Cu particle thickness versus Cu coverage at 100 K calculated from these ISS data points, and on the right axis, the average effective diameter of hemispherical caps that corresponds to this thickness. Also shown is the result expected for the same hemispherical-cap model and particle number density as used for the best fit to the data in part a.

to that for clean $CeO_{1.95}(111)$ before Cu deposition. The Cu ISS intensity increased with Cu coverage while the Ce ISS intensity decreased. As shown, the data deviate strongly from the layer-by-layer (2D) growth model but are well fit by the hemispherical cap (3D) model, which assumes Cu grows as hemispherical particles with a fixed particle diameter, D, at any coverage and a fixed number density of particles, n, independent of coverage.[35] The fixed density of particles is a well-known consequence of particle growth kinetics whereby a saturation density of clusters is formed at very low coverage and stays constant thereafter.[36] Because n and D are mathematically related for a given total Cu coverage, n is the only fitting parameter.[35] When the angle of detection is normal to the surface but the ions are incident at angle $\theta_i = 45°$ from normal, as here, that model gives that the fraction of the ceria substrate signal masked by Cu particles equals $n\pi D^2(1 + 1/\cos\theta_i)/8$,[37] $= (1.207)n\pi D^2/4$. The least-squares best fit shown in Figure 1a, gives $n = 5.3 \times 10^{13}$ particles/cm^2 for Cu adsorption onto $CeO_{1.95}(111)$ at 100 K. This is ~7 times as great as that observed for similarly prepared $CeO_{1.95}(111)$ surfaces and similar flux but at 300 K (7.8×10^{12} particles/cm^2).[29] The higher density is expected at 100 K because kinetic growth models appropriate for these conditions predict a saturation number density that varies as the inverse cube root of the Cu

DOI: 10.1021/acscatal.5b01372
ACS Catal. 2015, 5, 5673−5678

monomer diffusion constant across the surface,[36] which will be much smaller at 100 K than at 300 K. Within that model, this ratio of 7 corresponds to an activation energy for Cu monomer diffusion of ~7 kJ/mol on CeO_2(111).

To ensure no ion beam damage in Figure 1a, a growth experiment was performed with only two Cu coverages (1 and 2 ML), giving much less total ion beam exposure up to 2 ML. These data fell within error of Figure 1a, indicating that no ion-beam damage occurred.

The normalized ISS signals in Figure 1a directly provide the fraction of the ceria surface whose signal is masked by Cu particles and the fraction of the total maximum Cu signal (due to complete coverage by Cu) that is observed at any given Cu coverage. If we assume the masked area is expanded from the actual footprint of the Cu particles as a result of macroscopic shadowing by the same factor as for hemispherical caps ($(1 + 1/\cos\theta_i)/2 = 1.207$; see above), dividing these fractions by 1.207 gives the area fractions actually covered by Cu particles. Because we know the average Cu film thickness from the Cu coverage (assuming the Cu particles have the density of bulk Cu(solid)), dividing it by this covered fraction for each point gives the average thickness of the Cu particles. Figure 1b shows the average Cu particle thickness versus Cu coverage estimated in this way. These thicknesses would only decrease by 21% even if we assumed no macroscopic shadowing, so this hemispherical-shape assumption has only a small effect on the thickness plotted here. Because the average thickness of a hemispherical cap is 1/3 its diameter, we multiplied this thickness by 3 to show the corresponding average effective diameter along the right-hand axis here. For comparison, the result expected from the same hemispherical-cap model and particle number density as used for the best fit to the top part of Figure 1 shows excellent agreement. The XPS signals observed were also consistent with this hemispherical cap model[29] but much less surface-sensitive than ISS, so they are not presented. It is unlikely that the deposited Cu was incorporated into the ceria film as a dopant (i.e., substituting for a Ce atom) because of the high activation energy expected. (The energy cost to create a Ce vacancy is 1833 kJ/mol,[18] and surface Ce vacancies are absent in these as-prepared CeO_2(111) films.[33])

3.3. Heats of Cu Adsorption on $CeO_{1.95}$(111) at 100 K.

Figure 2 shows the heat of adsorption of Cu onto $CeO_{1.95}$(111) at 100 K and at 300 K from ref 29 as a comparison. All heats of adsorption reported here have been corrected slightly for the hot temperature and directed nature of the Cu atomic beam to correspond to Cu atoms in a Boltzmann distribution at the surface temperature, and RT has been subtracted from the measured energies, as we always do in calorimetry.[30−32] This is done so the values on plots such as Figure 2 (times −1) equal the standard enthalpy of adsorption at the sample temperature. At 100 K, Cu adsorbs with an initial heat of adsorption of 225 kJ/mol, remains nearly constant for the first two gas pulses, and then increases with coverage to asymptotically approach the standard heat of sublimation of bulk Cu(solid) (337 kJ/mol at 300 K[38] and 332 kJ/mol at 100 K[38]) by 5 ML. The sticking probability of Cu atoms was found to be unity at all coverages. As shown in Figure 2, the initial heat of adsorption of Cu on $CeO_{1.95}$(111) at 100 K is 75 kJ/mol lower than at 300 K and remains lower at all coverages. The Cu heat of adsorption on $CeO_{1.95}$(111) at 100 K converges to the heat of sublimation by 5 ML, which is slower than at 300 K. The difference in initial heats of adsorption is partially due to the smaller particles at 100 K (see below), but also partially due to the aggregation of Cu nanoparticles, primarily at step sites at 300 K[29] but on terraces at 100 K due to slower Cu adatom diffusion at 100 K (see below).

Using the particle density from the hemispherical cap model in Figure 1a and the total Cu coverage in Figure 2, the measured heats are replotted as Cu heat of adsorption vs average Cu particle diameter in Figure 3. Again, the Cu heat of adsorption on $CeO_{1.95}$(111) at 300 K from ref 29 is shown for comparison. The plot is truncated for nanoparticles larger than 0.85 nm at 100 K (equivalent to 1 ML total coverage) because the fractional surface covered reached 35%, above which the hemispherical cap model might begin to break down as a result of particles possibly overlapping each other. The heat of adsorption for Cu nanoparticles with a similar particle diameter in the range 0.45−0.8 nm is lower at 100 K than at 300 K because of different adsorption sites at the two temperatures (see below). The particle density determined from the fit to the

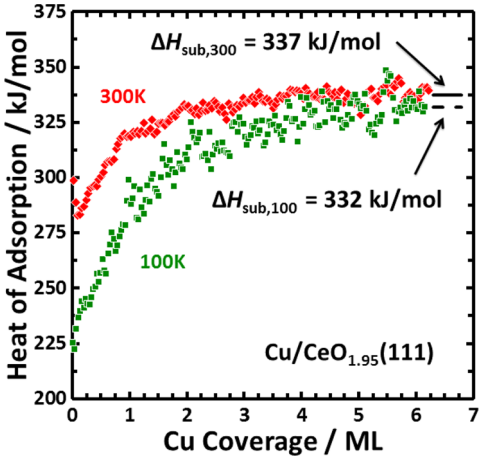

Figure 2. Cu atom heat of adsorption at 300 K (diamonds, from ref 29) and 100 K (squares) on $CeO_{1.95}$(111) as a function of Cu coverage.

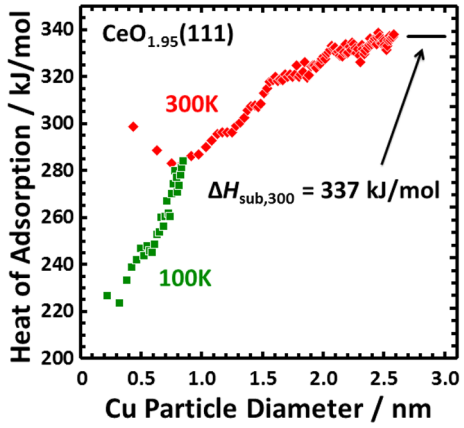

Figure 3. Cu atom heat of adsorption at 300 K (diamonds, from ref 29) and 100 K (squares) on $CeO_{1.95}$(111) as a function of average Cu particles diameter after adsorption. The effective particle diameter was calculated using the total Cu coverage, assuming the nanoparticles grow as hemispherical caps with a constant particle density of 5.3×10^{13} particles/cm^2. The data at 300 and 100 K were truncated at 35% total surface coverage to avoid heats when particles were agglomerating.

DOI: 10.1021/acscatal.5b01372
ACS Catal. 2015, 5, 5673−5678

hemispherical cap model is larger than the number of Cu atoms per unit area adsorbed in the first two gas pulses, indicating that these two calorimetry pulses produce only isolated Cu adatoms at 100 K. The effective hemispherical Cu particle diameter is 0.22 and 0.32 nm for these pulses, which correspond to particle volumes of 2.9×10^{-3} and 8.6×10^{-3} nm^3, respectively, both smaller than the volume per atom in bulk Cu(solid), 1.18×10^{-2} nm^3 based on its density.[38] This is, of course, impossible, which we attribute to a breakdown of the assumption of fixed density of nuclei at such low coverages. The nuclei here are single, isolated Cu adatoms, and their number density increases in these first two pulses. These two pulses gave the same heat of adsorption, within 3 kJ/mol, which does not increase with coverage (effective diameter) in this ultrasmall size range, as at larger sizes. This is again consistent with these two pulses' producing the same structure: isolated Cu adatoms on $CeO_2(111)$ terraces. These heats for isolated Cu adatoms average 224 kJ/mol. This value will allow for much more direct comparisons to DFT results than all our earlier calorimetry measurements of such systems, for which multiatom clusters of unknown geometry were made in the first gas pulse (see below). Figure 3 represents the first measurement of the heat of any metal adsorption on any oxide that covers the full size range from isolated metal adatoms to such large metal nanoparticles that they have reached the bulk limit.

Because Figure 3 presents *differential* heats of adsorption, these differences in heats of adsorption with size directly reflect differences with size in the chemical potential of the metal atoms, but with opposite sign. Neglecting entropic contributions to the free energy, which change very little with particle size compared with the huge enthalpic changes here, the chemical potential of a metal atom in a particle of diameter D, $\mu(D)$, is higher than that in the bulk metal, $\mu(\infty)$, by an amount equal to the heat of sublimation of bulk Cu minus the differential heat of Cu adsorption at diameter D.[13] Thus, another way to view the data from Figure 3 is to plot this chemical potential (relative to that for the bulk metal, $\mu(\infty)$, which we set as the reference zero here) versus average effective diameter, as shown in Figure 4. Here, we have corrected the first two data points at 100 K to reflect the proper effective hemisphere diameter of single, isolated atoms. As seen, these Cu adatoms at terrace sites are ~110 kJ/mol higher in chemical potential than Cu atoms in particles that have reached the large-size limit (>2.5 nm). This shows why it is challenging to make so-called single-site catalysts (i.e., isolated late transition metal adatoms on supports). This drop in chemical potential with size reflects the thermodynamic driving force for catalysts to sinter into larger particles with time on stream.[11,13] It also reflects a decreasing propensity for the metal to bind strongly to small adsorbates, mainly associated with the decreasing degree of coordinative unsaturation as size grows.[13] Also clear in Figure 4 is the large decrease in chemical potential of ~57 kJ/mol between Cu in dimers at step edges compared with dimers on terraces. Once the particles exceed 0.85 nm in diameter, this stabilization by step edges has diminished to an undetectable level.

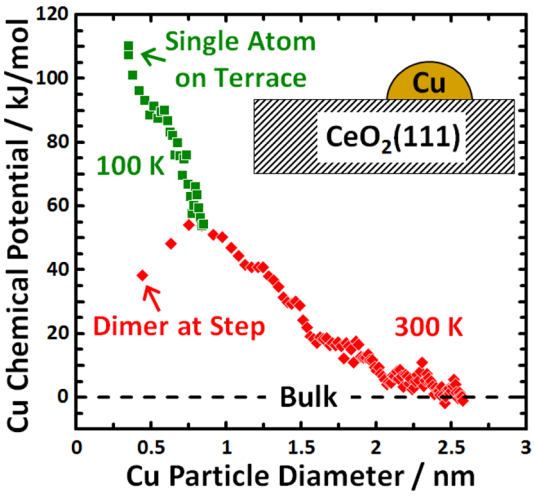

Figure 4. Chemical potential of Cu atoms in Cu nanoparticles on $CeO_{1.95}(111)$ relative to that in bulk Cu(solid) versus the effective diameter of the Cu particle down to the single atom limit.

4. DISCUSSION

In Figure 3, the difference in the heats of adsorption at 100 K versus 300 K for Cu on $CeO_{1.95}(111)$ for nanoparticles of the same size below 0.85 nm in diameter is attributed to differences in binding sites of the nanoparticles. Although there are no STM images available for Cu adsorption on $CeO_{1.95}(111)$, we have proposed that the majority of Cu atoms deposited at 300 K are nucleated into nanoparticles at step edges (including kink sites)[29] to explain adsorption heats and other data at 300 K for Cu on $CeO_{1.95}(111)$, most importantly the initial decrease in heat of adsorption with coverage and particle size (Figures 2, 3) as these step sites get titrated. (Particle-particle repulsions probably keep the steps from getting completely covered by particles.) This is consistent with STM results for similar systems (nanoparticles of Ag[39] and Au[23] on $CeO_2(111)$ and Cu on Al_2O_3[40] and $TiO_2(110)$[41] at 300 K).

When grown at 100 K, the particle density increases to ~7-fold compared to 300 K (5.3×10^{13} vs 7.8×10^{12} particles/cm^2, respectively). Similar increases in particle density were observed by Freund et al.[23,42] for Au on $CeO_2(111)$ at 100 versus 300 K, with the increased density at 100 K due to Au particles nucleated on terraces, as opposed to much more predominantly at steps at 300 K. The increased particle density for Cu/$CeO_{1.95}(111)$ at 100 K is also attributed to nucleation of Cu nanoparticles mainly on terraces, whereas they nucleate mainly on steps at 300 K.[29] This explains the 52 kJ/mol lower heat of adsorption at 100 K versus 300 K in Figure 3 for 0.44 nm diameter Cu particles (the smallest Cu nanoparticles measured at 300 K), given the well-known lower-stability metal nanoparticles on terraces compared with steps.[43,44] This difference in heats of adsorption slowly diminishes with size to zero by 0.85 nm, probably because the increasing footprint of the Cu particles is associated mainly with their expanding onto terraces above 0.85 nm, even when they started at step edges. The nanoparticles are probably not exclusively nucleated at steps for adsorption at 300 K nor terraces at 100 K, but these are their dominant nucleation sites.

Because this surface has 2.5% oxygen vacancies (mainly at step edges),[29] the Cu atoms may be located at a mixture of oxygen vacancies and stoichiometric ceria sites. However, because DFT results from both Fabris et al.,[17] and Hermansson et al.[18] predicted that Cu binds 1.4−1.2 eV (135 and 116 kJ/mol) more strongly to stoichiometric ceria sites on (111) terraces than to oxygen vacancies in (111) terraces, consistent with our experimental result that Cu in 0.4 nm diameter particles is ~40 kJ/mol less stable on the more reduced $CeO_{1.8}(111)$ surface than on $CeO_{1.95}(111)$,[29] the isolated Cu

DOI: 10.1021/acscatal.5b01372
ACS Catal. 2015, 5, 5673−5678

Table 1. Calculated Heats of Adsorption of Isolated Cu Adatoms on the Most Stable Cu Adsorption Site of $CeO_2(111)$ Using DFT + U Compared to the Experimental Value, and the Deviations from This Experiment[a]

ΔH_{ad} (kJ/mol)	ΔH_{ad} error (kJ/mol)	Cu charge	DFT functional	U (eV)	slab thickness (trilayers)	source
224 ± 7			experiment			this work
293	69	1+	PBE	4.5	3	17
260	36	0.66+	PBE	5	3	18
254	30	1+	PBE	4.5	4	19
259	35	0.67+	PBE	5	2	20
180	−44	0.70+	PW91[b]	5 then 3[b]	2	21[b]
270	46	0.71+	PW91	5		
336	112		LDA	5		

[a]To correct for the difference between enthalpies and energies, 0.8 kJ/mol (RT) was added to the calculated energies. Also listed are the U value and slab thickness used in each calculation and the resulting charge on the Cu adatom. All calculations used a 2 × 2 cell. One trilayer is defined as an O−Ce−O trilayer. [b]Illas et al.[21] pointed out that GGA tends to overestimate the $CeO_2(111)$ lattice parameter, so they used the local density approximation (LDA) with the functional of Vosko et al.[45] with U = 5 for geometry optimization but used GGA with the Pedrew−Wang (PW91)[46] functional and U = 3 for energy and electronic calculations. They also performed pure GGA and LDA calculations for comparison, listed in the last two rows here.

adatoms produced here at 100 K on terraces surely adsorb only to stoichiometric sites and avoid bonding to oxygen vacancies. At 300 K, Cu diffuses fast enough to reach step edges, where it binds more strongly than at terraces despite these steps missing about half of their oxygens.[29]

These results provide benchmarks to test the energy accuracy of computational estimates of metal bonding to oxide surfaces. Table 1 compares the measured adsorption energy for Cu adatoms on stoichiometric $CeO_2(111)$ with published DFT + U results at its most stable adsorption geometry (using periodic boundary conditions within the generalized gradient approximation (GGA)[44]). To properly describe the localization of the Ce 4f electrons, a Hubbard parameter (U) was added to the functionals, as summarized in Table 1.[25−27] These calculated Cu adsorption energies are generally higher by 30−69 kJ/mol than our experimental result. Because the heat capacity of solids is generally smaller than gases at low temperature, part of this difference may be due to the fact that the calculation is at 0 K, whereas the measurement is at 100 K. This could account for only <2.1 kJ/mol of the difference because the average heat capacity difference is surely less than the heat capacity of Cu(gas) (5/2 R). This main difference can be associated with the use of large U values. The result by Illas et al.[21] using a lower U (3 eV) is the only calculation to underestimate the adsorption energy, although the magnitude of the error is not improved. Huang et al.[28] showed that calculated adsorption energies for CO on $CeO_2(111)$ were better represented using lower U values (2−3 eV) and suggested that a lower U is probably required whenever describing electron transfer reactions. Also listed in Table 1 are the charge transfers predicated by DFT, which are generally >+0.66. Using the PBE + 4.5 functional, the calculated charge transfer is greater than PBE + 5; however, PW91 gives a similar extent of charge transfer, independent of U value. Our XPS results[29] indicate only a small amount of electron density is transferred from Cu to $CeO_{1.95}(111)$, approximately 0.17 electrons per Cu atom at 1.2 ML Cu coverage.[29] However, when analyzed in this same way, the data of Matolin et al.[24] on $CeO_{1.99}(111)$ give 0.62 electrons per Cu atom up to 0.6 ML Cu, after which it tracks our data. It thus seems that all these DFT functionals are overestimating the extent of charge transfer, although the charge transfer per Cu atom is not known from experiments at the very low coverage and temperature required to maintain isolated Cu adatoms.

5. CONCLUSIONS

Copper atoms adsorb onto $CeO_{1.95}(111)$ at 100 K with a nearly constant heat of adsorption of 224 kJ/mol at very low coverage, associated with Cu adatoms on stoichiometric terrace sites. Above 0.05 ML, Cu grows as 3D Cu nanoparticles on $CeO_{1.95}(111)$ at 100 K, with a fixed particle density of 5.3 × 10^{13} particles/cm^2, 7-fold as large as at 300 K The heat of adsorption increases slowly with coverage (and particle size) to eventually reach the heat of sublimation of bulk Cu(solid). The heat of Cu adsorption when making Cu nanoparticles with an average diameter of 0.45 to 0.8 nm is lower at 100 K than at 300 K by ∼50−30 kJ/mol on the same $CeO_{1.95}(111)$ surface, attributed to cluster nucleation on terrace sites at 100 K but instead on the more stable step edge sites at 300 K. Figure 4 summarizes the measured chemical potential of Cu atoms versus Cu nanoparticle size at both stoichiometric $CeO_2(111)$ terraces and step edges with ∼50% oxygen vacancies. Because Cu is much less stable near oxygen vacancies on this surface,[29] it will avoid bonding near oxygen vacancies upon adsorption. Thus, the results for the smallest Cu clusters in Figure 1 are not strongly influenced by the ∼2.5% oxygen vacancies present on this CeO_2 surface. We therefore consider the monomer and dimer energies in Figure 4 to be representative of stoichiometric $CeO_2(111)$. Comparison to DFT + U calculations shows that calculated monomer adsorption energies differ from this experiment by −44 to +69 kJ/mol.

AUTHOR INFORMATION

Corresponding Author

*Phone: 206-616-6085. E-mail: campbell@chem.washington.edu.

Notes

The authors declare no competing financial interest.

ACKNOWLEDGMENTS

The authors acknowledge the Department of Energy, Office of Basic Energy Sciences, Chemical Sciences Division Grant No. DE-FG02-96ER14630 for support of this work.

REFERENCES

(1) Freund, H. J. *Surf. Sci.* **2002**, *500*, 271−299.
(2) Chen, M. S.; Goodman, D. W. *Science* **2004**, *306*, 252−255.
(3) Herzing, A. A.; Kiely, C. J.; Carley, A. F.; Landon, P.; Hutchings, G. J. *Science* **2008**, *321*, 1331−1335.

DOI: 10.1021/acscatal.5b01372
ACS Catal. 2015, 5, 5673−5678

(4) Vajda, S.; Pellin, M. J.; Greeley, J. P.; Marshall, C. L.; Curtiss, L. A.; Ballentine, G. A.; Elam, J. W.; Catillon-Mucherie, S.; Redfern, P. C.; Mehmood, F.; Zapol, P. *Nat. Mater.* **2009**, *8*, 213−216.
(5) Lee, I.; Delbecq, F.; Morales, R.; Albiter, M. A.; Zaera, F. *Nat. Mater.* **2009**, *8*, 132−138.
(6) Graciani, J.; Mudiyanselage, K.; Xu, F.; Baber, A. E.; Evans, J.; Senanayake, S. D.; Stacchiola, D. J.; Liu, P.; Hrbek, J.; Fernandez Sanz, J.; Rodriguez, J. A. *Science* **2014**, *345*, 546−550.
(7) Behrens, M.; Studt, F.; Kasatkin, I.; Kuehl, S.; Haevecker, M.; Abild-Pedersen, F.; Zander, S.; Girgsdies, F.; Kurr, P.; Kniep, B.-L.; Tovar, M.; Fischer, R. W.; Norskov, J. K.; Schloegl, R. *Science* **2012**, *336*, 893−897.
(8) Hansen, P. L.; Wagner, J. B.; Helveg, S.; Rostrup-Nielsen, J. R.; Clausen, B. S.; Topsoe, H. *Science* **2002**, *295*, 2053−2055.
(9) Pacchioni, G. *Phys. Chem. Chem. Phys.* **2013**, *15*, 1737−1757.
(10) Matthey, D.; Wang, J. G.; Wendt, S.; Matthiesen, J.; Schaub, R.; Laegsgaard, E.; Hammer, B.; Besenbacher, F. *Science* **2007**, *315*, 1692−1696.
(11) Farmer, J. A.; Campbell, C. T. *Science* **2010**, *329*, 933−936.
(12) Campbell, C. T. *Acc. Chem. Res.* **2013**, *46*, 1712−1719.
(13) Campbell, C. T.; Sellers, J. R. V. *Faraday Discuss.* **2013**, *162*, 9−30.
(14) Campbell, C. T. *Science* **2004**, *306*, 234−235.
(15) Campbell, C. T.; Parker, S. C.; Starr, D. E. *Science* **2002**, *298*, 811−814.
(16) Campbell, C. T.; Peden, C. H. F. *Science* **2005**, *309*, 713−714.
(17) Szabova, L.; Camellone, M. F.; Huang, M.; Matolin, V.; Fabris, S. *J. Chem. Phys.* **2010**, *133*, 234705.
(18) Yang, Z. X.; He, B. L.; Lu, Z. S.; Hermansson, K. *J. Phys. Chem. C* **2010**, *114*, 4486−4494.
(19) Tang, Y. H.; Zhang, H.; Cui, L. X.; Ouyang, C. Y.; Shi, S. Q.; Tang, W. H.; Li, H.; Chen, L. Q. *J. Power Sources* **2012**, *197*, 28−37.
(20) Yang, Z.; Xie, L.; Ma, D.; Wang, G. *J. Phys. Chem. C* **2011**, *115*, 6730−6740.
(21) Branda, M. M.; Hernandez, N. C.; Sanz, J. F.; Illas, F. *J. Phys. Chem. C* **2010**, *114*, 1934−1941.
(22) Migani, A.; Vayssilov, G. N.; Bromley, S. T.; Illas, F.; Neyman, K. M. *Chem. Commun.* **2010**, *46*, 5936−5938.
(23) Lu, J. L.; Gao, H. J.; Shaikhutdinov, S.; Freund, H. J. *Catal. Lett.* **2007**, *114*, 8−16.
(24) Szabova, L.; Skala, T.; Matolinova, I.; Fabris, S.; Farnesi Camellone, M.; Matolin, V. *Appl. Surf. Sci.* **2013**, *267*, 12−16.
(25) Fabris, S.; Vicario, G.; Balducci, G.; de Gironcoli, S.; Baroni, S. *J. Phys. Chem. B* **2005**, *109*, 22860−22867.
(26) Castleton, C. W. M.; Kullgren, J.; Hermansson, K. *J. Chem. Phys.* **2007**, *127*, 244704.
(27) Andersson, D. A.; Simak, S. I.; Johansson, B.; Abrikosov, I. A.; Skorodumova, N. V. *Phys. Rev. B: Condens. Matter Mater. Phys.* **2007**, *75*, 035109.
(28) Huang, M.; Fabris, S. *J. Phys. Chem. C* **2008**, *112*, 8643−8648.
(29) James, T. E.; Hemmingson, S. L.; Ito, T.; Campbell, C. T. *J. Phys. Chem. C* **2015**, *119*, 17209−17217.
(30) Sellers, J. R. V.; James, T. E.; Hemmingson, S. L.; Farmer, J. A.; Campbell, C. T. *Rev. Sci. Instrum.* **2013**, *84*, 123901.
(31) Stuckless, J. T.; Frei, N. A.; Campbell, C. T. *Rev. Sci. Instrum.* **1998**, *69*, 2427−2438.
(32) Stuckless, J. T.; Frei, N. A.; Campbell, C. T. *Sens. Actuators, B* **2000**, *62*, 13−22.
(33) Farmer, J. A.; Baricuatro, J. H.; Campbell, C. T. *J. Phys. Chem. C* **2010**, *114*, 17166−17172.
(34) Romeo, M.; Bak, K.; Elfallah, J.; Lenormand, F.; Hilaire, L. *Surf. Interface Anal.* **1993**, *20*, 508−512.
(35) Diebold, U.; Pan, J. M.; Madey, T. E. *Phys. Rev. B: Condens. Matter Mater. Phys.* **1993**, *47*, 3868−3876.
(36) Venables, J. A. *Surf. Sci.* **1994**, *299*, 798−817.
(37) Campbell, C. T.; James, T. E. *Surf. Sci.* **2015**, *641*, 166−169.
(38) *CRC Handbook of Chemistry and Physics*; 95th ed.; Haynes, W. M., Ed.; CRC Press: Boston, 2014, pp 4−124, 5−10, 12−206.
(39) Hu, S.; Wang, Y.; Wang, W.; Han, Y.; Fan, Q.; Feng, X.; Xu, Q.; Zhu, J. *J. Phys. Chem. C* **2015**, *119*, 3579−3588.
(40) Worren, T.; Højrup Hansen, K.; Laegsgaard, E.; Besenbacher, F.; Stensgaard, I. *Surf. Sci.* **2001**, *477*, 8−16.
(41) Chen, D. A.; Bartelt, M. C.; Hwang, R. Q.; McCarty, K. F. *Surf. Sci.* **2000**, *450*, 78−97.
(42) Baron, M.; Bondarchuk, O.; Stacchiola, D.; Shaikhutdinov, S.; Freund, H. J. *J. Phys. Chem. C* **2009**, *113*, 6042−6049.
(43) Barth, J. V.; Costantini, G.; Kern, K. *Nature* **2005**, *437*, 671−679.
(44) Perdew, J. P.; Burke, K.; Ernzerhof, M. *Phys. Rev. Lett.* **1996**, *77*, 3865−3868.
(45) Vosko, S. H.; Wilk, L.; Nusair, M. *Can. J. Phys.* **1980**, *58*, 1200−1211.
(46) Perdew, J. P.; Chevary, J. A.; Vosko, S. H.; Jackson, K. A.; Pederson, M. R.; Singh, D. J.; Fiolhais, C. *Phys. Rev. B: Condens. Matter Mater. Phys.* **1992**, *46*, 6671−6687.

DOI: 10.1021/acscatal.5b01372
ACS Catal. 2015, 5, 5673−5678